Innovative process to obtain thin films and micro-nanostructured ZrN films from a photo-structurable ZrO2 sol-gel using rapid thermal nitridation

V. Vallejo-Otero, N. Crespo-Monteiro, A. Valour, C. Donnet, S. Reynaud, N. Ollier, M.F. Blanc Mignon, J.P. Chatelon, Y. Bleu, E. Gamet, et al.

Materials Today Advances 20 (2023) 100430

Contents lists available at ScienceDirect

Materials Today Advances

journal homepage: www.journals.elsevier.com/materials-today-advances/

Innovative process to obtain thin films and micro-nanostructured ZrN films from a photo-structurable ZrO_2 sol-gel using rapid thermal nitridation

V. Vallejo-Otero, N. Crespo-Monteiro *, A. Valour, C. Donnet, S. Reynaud, N. Ollier, M.F. Blanc Mignon, J.P. Chatelon, Y. Bleu, E. Gamet, Y. Jourlin

Université Jean Monnet Saint-Etienne, CNRS, Institut d'Optique Graduate School, Laboratoire Hubert Curien UMR 5516, F-42023, Saint-Etienne, France

ARTICLE INFO

Keywords:
Zirconium nitride
Sol-gel method
Rapid thermal nitridation
Optical properties
Micro-nanostructuring

ABSTRACT

Zirconium nitride (ZrN) is widely used in many industrial sectors for its outstanding performances including its mechanical properties, high chemical and thermal stability. Associated with its plasmonic behavior, these properties make ZrN a suitable candidate for optical applications at high temperature or in extreme environments. The authors present an innovative, easy-to-use and rapid process for producing ZrN thin films from a photo-structurable ZrO_2 sol-gel using a rapid thermal nitridation (RTN) process. In this process, a ZrO_2 sol-gel layer is converted into a ZrN thin film in a few minutes by rapid thermal annealing (RTA) under ammonia gas. Compared to physical or chemical vapor deposition, usually used to produce ZrN thin films, the advantages of the sol-gel method include suitability for non-planar and large substrates and the possibility of nanotexturing of crystallized ZrN surfaces in considerably less time, at a larger scale and at a lower cost. The ZrO_2 and ZrN thin films were characterized by Raman spectroscopy, X-ray diffraction and Transmission Electron Microscopy, to confirm complete nitridation. The optical, electrical and tribological properties were also investigated. Finally, the nitridation method was also used on structured ZrO_2 layers and showed the versatility of the process e.g. enabling the production of micro-nanostructured ZrN films without using any etching techniques.

1. Introduction

Zirconium nitride (ZrN) has attracted considerable attention in recent years, in particular for its plasmonic behavior in the visible-NIR region [1–3]. In addition to its interesting plasmonic properties, ZrN has outstanding mechanical performances (hardness and Young's modulus are around 20 GPa and 350 GPa respectively); resistance to corrosion and oxidation; low resistivity (around 50 μΩ cm) and high thermal stability (melting point is around 2800 °C) [4–6]. ZrN thin film is usually produced by vapor deposition techniques in advanced vacuum such as atomic layer deposition (ALD) [7,8], chemical vapor deposition (CVD, MOCVD, PECVD) [9–13], ion-plated [14], magnetron sputtering [15–17], vacuum arc deposition [18,19], under ammonia or nitrogen atmosphere. Different zirconium sources can be used for each technique: in the case of the physical vapor deposition techniques (PVD) Zr target is used [14–19], for CVD techniques, ZrN can be synthesized from zirconium chloride [7,9,11,12], tetrakis dimethylamido zirconium (TDMAZr) [8], tetrakis(diethylamido)zirconium $Zr[N(C_2H_5)_2]_4$ [10] and tetrakis(ethylmethylamino) zirconium $[Zr(NMeEt)_4]$ [13]. Even though these deposition techniques are widely used, they are expensive and time consuming. Furthermore, these techniques make structuring very difficult due to the mechanical and electrical properties of ZrN. An alternative to these deposition techniques is the nitridation of ZrO_2. To our knowledge, very few studies were conducted on this subject to date [20,21]. Bo Fu et al. worked on the nitridation of ZrO_2 powder in NH_3 flow gas using Mg as a reductant and successfully produced ZrN powder using a 6-h heat treatment at 1000 °C. Yamamura et al. successfully synthesized ZrN thin film using carbothermal nitridation with a ZrO_2 sol-gel. This process of nitridation involves the conversion of ZrO_2 into ZrN by reduction and nitridation in a carbon crucible at 1400 °C for 1 h in a nitrogen atmosphere in which the carbon crucible acts as a reductant. In the current state of the art, nitridation of ZrN requires a long reaction time at high temperature with a reductant. In previous studies, we succeeded in obtaining obtain titanium nitride (TiN) thin film using an innovative Rapid Thermal Nitridation (RTN) technique with ammonia gas and a titanium oxide (TiO_2) photo-structurable sol-gel [22–24]. In this paper, we present a new RTN process that produces ZrN from a ZrO_2 photo-structurable sol-gel by nitridation with ammonia gas.

* Corresponding author.
E-mail address: nicolas.crespo.monteiro@univ-st-etienne.fr (N. Crespo-Monteiro).

https://doi.org/10.1016/j.mtadv.2023.100430
Received 18 July 2023; Received in revised form 22 September 2023; Accepted 23 September 2023
Available online 29 September 2023

The process requires neither extended firing time nor additional reductant. It is a very versatile technique enabling rapid, easy and inexpensive production of ZrN thin film. The micro-nanostructuring of the ZrN layer is also a challenge. Indeed, few authors have reported processes to pattern ZrN films. E-beam lithography and dry etching [25] or scanning probe microscopy oxidation and hydrofluoric acid etching [26] were used for this purpose, but these techniques are time consuming, use toxic products, and are expensive. Conversely, sol-gel ZrO_2 can be easily structured by UV exposure [27], thereby making it possible to create ZrN micro-nanostructured thin films with complex shapes after nitridation.

In this paper, ZrN films are characterized before and after nitridation. This conversion is first accessed by UV–visible-near-IR spectroscopy. The structural properties are then measured by RAMAN spectroscopy, X-ray diffraction and by High-Resolution Transmission Electron Microscopy (HRTEM) and Electron Energy Loss Spectroscopy (EELS) analysis. Optical measurements are made by spectroscopic ellipsometry. Electrical properties are estimated using the four-point probe method. The mechanical properties of the films produced by this process are tested in friction with a linear reciprocating tribometer, then compared with the properties reported in the literature (ZrN obtained using conventional deposition process such as PVD, CVD and ALD). This treatment is also applied to structured films of ZrO_2. Micro-nanostructures of ZrN are presented and their pattern quality and dimensions are compared before and after nitridation using Atomic Force Microscopy (AFM) measurements and Scanning Electron Microscope (SEM) measurements.

2. Material and methods

2.1. Elaboration of the ZrO_2 sol-gel layer

The process used to produce the sol-gel was previously published [27]. Briefly, the ZrO_2 sol-gel was prepared from a mixture of two sols at room temperature. The first sol was prepared by reacting Zirconium (IV) propoxide ($Zr(OPr)_4$ from Fluka) with 1-Benzoylacetone (BzAc from Aldrich) in anhydrous ethyl alcohol (EtOH from Aldrich). This first sol gives the photosensitive properties to the sol-gel thanks to the BzAc. The $Zr(OPr)_4$/BzAc/EtOH molar composition was 1/0.9/20. The second sol was prepared by mixing $Zr(OPr)_4$ with deionized water, hydrochloric acid (HCl from Roth), and butyl alcohol (BuOH from Merck) as a solvent, the role of this sol is to introduce the species that control the reaction kinetics in order to have a good gelation after deposition. The $Zr(OPr)_4$ concentration in the solution was 0.4 M, and the $Zr(OPr)_4/H_2O$/HCl/-BuOH molar composition was 1/0.8/0.13/24. The two sols are kept separated for conservation matter. Indeed, once mixed the final product obtained can age or precipitated in about a week while separated the sols can be used for several months. The photo-structurable solution was prepared by mixing the first and the second sols to obtain a final sol with a $Zr(OPr)_4$ concentration of 0.6 M and a BzAc/$Zr(OPr)_4$ M ratio of 0.6.

The sol was then deposited on a silica glass substrate using a spin-coater at a speed of 3000 rpm for 30 s, before being heated at 110 °C for 90 min, this resulted in a xerogel film (we use the name ZrO_2 xerogel for the rest of this paper).

2.2. Rapid thermal nitridation of ZrO_2 xerogel thin film

A rapid thermal nitridation treatment was performed on the ZrO_2 xerogel thin layers in a reproducible and uniform process using NH_3 gas (99.98% purity). Nitridation occurs at high temperatures in a halogen infrared lamp-heated furnace (RTA As-One 100 from Annealsys). After a purge of the reactor with Argon (99.9999% purity) and vacuum sealing, the samples underwent 10 cycles, each cycle including 30 s of high irradiation (45% of the lamp power) and 5 s of low irradiation (1% of the lamp power). The high and low irradiation cycles protect the lamps from premature dysfunction. During the nitridation process a flow of NH_3 (1000 sccm) was introduced in the chamber at a pressure of 10 mbar. These nitridation parameters are based on previous studies of rapid thermal nitridation of TiO_2 [22,23]. They were adapted for the nitridation of ZrO_2 xerogel in this study but more optimal conditions may be possible. The infrared light is directly irradiating the sample without any susceptor as intermediary, thus only the surface of the sample gets heated up by absorption of the infrared flash light. The setup of this rapid thermal nitridation makes it very difficult the measurement of the temperature. We are currently working on a simulation of the heat transfer in order to have approximation of the reaction temperature.

This technique allows to produce homogeneous ZrN layers of thickness of 40–50 nm in a single step. If thicker films are required it is possible to stack the ZrN layers. The process consisted of deposition and nitridation of ZrO_2 xerogel multiple times on the same sample. In this article, samples with 3 layers were produced for the purpose of characterization by spectroscopic ellipsometry and to measure the resistivity. This sample is an example to show the possibility of this technique and to compare the properties of a thicker ZrN with the literature. The disadvantage of this technique is that it can induce different properties at the interfaces of the layers, and should be studied further in another study.

2.3. Optical measurements

Spectrophotometric measurements were taken before and after nitridation (Cary 5000 UV–Vis–NIR from Agilent Technologies). The measurements were performed in the *wavelength* range *between 200* and 2000 nm, in reflectance with an angle of incidence of 10° and in transmittance with normal incidence. The thickness, the refractive index (n) and the extinction coefficient (k) were measured by ellipsometry (SEMILAB Sopra GES-5E). The measurements were taken using an angle of incidence of 70° between 300 and 1000 nm. The optical model consists of 2 layers on a semi-infinite silica glass substrate. The first layer is made of the material under consideration (ZrO_2 or ZrN with porosity). The second layer is considered as a roughness layer, with a 50%–50% mixed dielectric function between void and the dielectric function of the first layer, as it can be schematized in Fig. 1. The dispersive law used for modelling the complex dielectric function of ZrO_2 xerogel layer is a Tauc-Lorentz model [28,29]. The imaginary part of the ZrO_2 dielectric function can be given as:

$$\varepsilon''(E) = \begin{cases} \frac{1}{E}\,\frac{AE_0C(E-E_g)^2}{(E^2-E_0^2)^2+C^2E^2}, E > E_g, \\ 0, E \le E_g, \end{cases}$$

where A is the amplitude, E_0 the energy and C the broadening of the oscillator and E_g is the bandgap of the material. The real part ε' of the ZrO_2 dielectric function is derived from the expression of ε'' using the Kramers-Kronig integration:

$$\varepsilon'(E) = \varepsilon_\infty + \frac{2}{\pi}.P\int_{E_g}^{\infty}\frac{\zeta.\varepsilon''(\zeta)}{\zeta^2-E^2}.d\zeta$$

where ε_∞ is the high frequency dielectric constant and P the Cauchy principal part of the integral.

For the complex dielectric function of ZrN material, we used a classical dispersion model based on the sum of a Drude and 2 Lorentz oscillators to create the dispersive law [30–32]. The expression of the complex dielectric function is presented thereafter:

$$\varepsilon(E) = \varepsilon'(E) + i.\varepsilon''(E) = \varepsilon_\infty - \frac{E_p^2}{E^2 + i\,E_\Gamma E} + \sum_{n=1}^{2}\frac{f_n E_n^2}{E_n^2 - E^2 + i\,\Gamma E}$$

where E_p and E_Γ are respectively the plasma energy and the broadening of the Drude model and f_n, E_n and Γ are respectively the strength, the position and the width of the nth oscillatorof the Lorentz model.

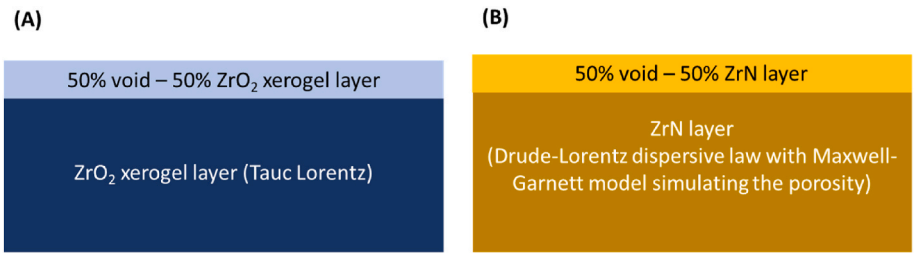

Fig. 1. Schematic diagram of the optical ellipsometry model for (A) the ZrO_2 xerogel layer and (B) the ZrN layer.

We used effective medium models to modelize the porosity and the roughness of the ZrN films: The Maxwell-Garnett model was used to modelized the porosity of the ZrN layer [33] and the Bruggeman model for the surface roughness of the same films [34]."

Film thickness of the ZrN 1-layer was also measured with a Veeco Dektak 3 ST profilometer.

2.4. Structural measurements

The composition of the film was analyzed before and after nitridation using RAMAN microspectroscopy (LabRam ARAMIS) with excitation at 633 nm.

Grazing incidence X-ray diffraction (GIXRD) was used to obtain a surface sensitive diffraction signal representative of the crystalline structures of the Zr-based thin films. The measurements were obtained using a PANalytical AERIS diffractometer. The X-ray beam used is produced by a copper anti-cathode with a wavelength of 0.154 nm and a power of 450W (15 mA, 30 kV). The acquisition was performed between $2\theta = 30°$ and $2\theta = 90°$, with a step size of 0.04°. ZrN grain size was estimated by quantifying the broadening of the diffraction peak widening, after subtracting the instrumental peak broadening deduced from the diffraction patterns of a calibrated LaB6 powder used as reference and analyzed under similar conditions.

Electron microscopy was used for both structural and chemical investigations. The process involved extracting focused ion beam (FIB) lamellas cut from the edge of a sample of non-nitridated ZrO_2 xerogel and a sample of nitridated ZrO_2 xerogel using a FEI Helios 600i dual-beam FIB/scanning electron microscopy (SEM). To be sure the probed volume was similar in ZrO_2 xerogel and ZrN, the thickness of the ZrO_2 xerogel sample was reduced from 250 nm to 100 nm by increasing the speed of the spin-coater to 8000 rpm for 30 s. The lamellas were then thinned at varying Ga + ion voltages and currents, and cleaned down to 1 kV to eliminate ion beam artifacts, such as redeposition or amorphization. Subsequently, TEM and HR-TEM images of the lamellas were acquired using a JEOL Neo-ARM 200F TEM equipped with a spherical aberration corrector, operating at acceleration voltages of 200 kV. EELS and high angle annular dark field (HAADF)-STEM experiments were performed using a Gatan imaging filter (GIF Quantum ER) and a Gatan ADF STEM detector. STEM-EELS data sets were acquired using the spectrum imaging (SI) technique. Spectra and elemental maps were extracted from dual-EELS SI raw data using DM software.

2.5. Electrical measurements

Resistivity measurements were performed with the 4-point probe method using the Microworld Lucas system. The spacing between each point was 1 mm, the weight applied was about 440 mN and the radius of the point was 254 μm. The surface resistance of each sample was measured at 10 different locations and then the mean value of resistivity was computed.

2.6. Friction measurements

To test the friction resistance of the ZrN film, tribological measurements were performed with a linear reciprocating tribometer (Phoenix TE79) in ambient air (relative humidity 65%) at room temperature (22 °C). The ZrN film deposited on a silica glass substrate was in sliding contact with a mirror polished AISI 52100 steel ball (diameter 6 mm) at a linear speed of 1 mm s^{-1} along a 3 mm wear track length. A normal force of 1 N was applied in the contact, consistent with mean and maximum Hertzian contact pressures of 266 and 400 MPa, respectively, and a Hertzian contact diameter of 70 μm.

2.7. Photo-structuring process

The ZrO_2 xerogel can be structurally modified on a micro-nano scale by employing UVA illumination at 365 nm. The xerogel films is soluble in various solvents including alcohol, chloroform, and acetone, as long as the TIPT-BzAc complex remains intact. However, when irradiated with UVA light, the TIPT-BzAc complex in the xerogel layer undergoes partial degradation, resulting in the formation of insoluble species such as carbonates and/or carboxylates. By precisely controlling the spatial distribution of illuminated and non-illuminated regions, it is possible to generate a patterned ZrO_2 xerogel layer. Subsequently, the exposed film is developed by immersion in ethanol, followed by a deionized water rinse. The ethanol dissolves the non-illuminated areas, while the water is used to stabilize the layer. Ultimately, the resulting pattern corresponds to the region exposed to UVA illumination.

After deposition of the ZrO_2 xerogel on the SiO_2 substrate (Fig. 2A) silica microspheres with a diameter of 2.5 μm, suspended in a 95% v/v ethanol solution and functionalized with a hydrophobic surface, were deposited using the Langmuir-Blodgett (LB) approach (Fig. 2B). The LB deposition was performed using a KSV NIMA LB machine (Biolin Scientific). The silica microspheres monolayer was spread on the aqueous sub-phase at room temperature and left for 10 min to allow evaporation of the solvent. The compression of the monolayer was carried out at a barrier speed of 3 mm min^{-1}, and then LB deposition on the thin film was performed at a surface pressure of 40 mN m^{-1} using the dipping method with a withdrawal speed of 3 mm min^{-1}. The monolayer deposited present a 2D hexagonal arrangement (Fig. 2C) with a period of 2.5 μm ± 0.2 μm as it can be seen in the SEM image in Fig. 2F. Finally, the microspheres were illuminated at a wavelength of 365 nm for 120 s at an intensity of 105 mW cm^{-2} (Fig. 2D). Each microsphere of the monolayer behaves like a micro-lens by focusing incident UV light and creates a photonic nano-jet that emerges from the sphere in the ZrO_2 layer. The exposed film was then developed by immersing it in ethanol for a few seconds, and rinsing it in deionized water to obtain a 2D hexagonal arrangement of the ZrO_2 xerogel nanopillars (Fig. 2E).

3. Results and discussion

3.1. Characterization of the nitridation process

The ZrO_2 sol-gel was deposited by spin coating and thermally treated at 110 °C to get rid of the solvent. After deposition, the ZrO_2 xerogel layers are homogeneous and are about 250 nm thick (measured with the profilometer), they are visually transparent and colorless as can be seen in the inset of Fig. 3A. Their UV–Visible–NIR transmittance spectra are

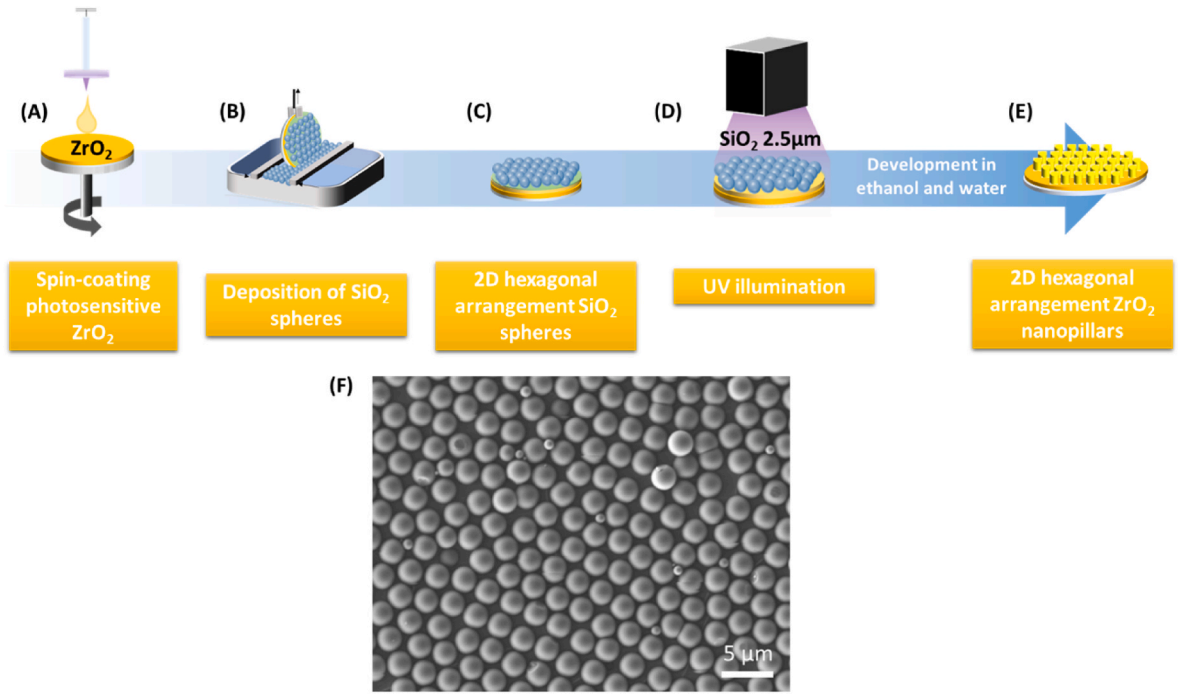

Fig. 2. (A, B, C, D, E) Schematic illustration of the colloidal lithography process. (F) SEM image of the silica monolayer (2.5 µm diameter).

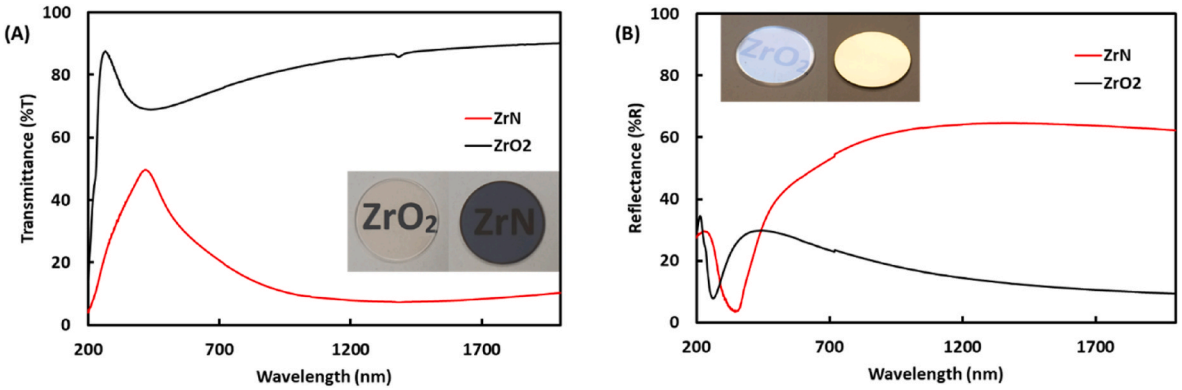

Fig. 3. UV–visible–NIR transmittance (A) and reflectance (B) spectra of ZrO_2 xerogel and ZrN thin films. Inset: (A) and (B) optical photographs of the same ZrO_2 xerogel and ZrN thin films in transmission and specular reflections, respectively.

characterized by a transmission over 80% at wavelengths higher than 400 nm, indicating good transparency in these regions (black curve in Fig. 3A). A significant absorption characteristic of the ZrO_2 xerogel occurs for UV wavelength [35,36]. Reflectance drops from more than 30% to slightly less 10% between 200 nm and 2000 nm (black curve in Fig. 3B). These results explain the bluish reflective color of the ZrO_2 xerogel layer (inset in Fig. 3B). After nitridation, transmittance is about 50% at 400 nm and decreases strongly under 10% in the near infrared wavelength (red curve in Fig. 3A). A marked increase in reflectance in the visible and in the near infrared wavelength is visible (red curve in Fig. 3B). The ZrN layer reflects up to 65% at 1500 nm and presents minimum reflectance (4%) at 350 nm. The film takes on a goldish reflective color but stays slightly transparent due to its low thickness (about 40 nm according to the measurement with the profilometer) (insets of Fig. 3A and B). As it can be seen from the measurements of the thicknesses by profilometry (250 nm before nitridation and 40 nm after nitridation) the RTN cause a shrinkage of the film due to its densification [22]. Indeed, the sol-gel film undergoes a process of nitridation where some of the species, such as the solvent and organic components, are eliminated, resulting in the film undergoing densification of about 85% in volume and a notable decrease in porosity.

Before nitridation, the Raman spectrum of ZrO_2 xerogel displayed none of the strong peaks of any form of crystallized ZrO_2 (black curve in Fig. 4) [37]. However, two strong peaks appeared at 1601 and 1005 cm^{-1}. They were attributed to 8b and 12 vibration modes of the phenyl group of BzAc. The two other peaks at 1302 and 1315 cm^{-1} can be attributed to C=C=C symmetric vibrations in chelating rings [38]. The other weaker peaks were assumed to be related to the BzAc or ZrO_2/BzAc complex.

After nitridation, the spectrum (in red in Fig. 4), displayed three distinct bands at frequencies 168 cm^{-1}, 216 cm^{-1} and 492 cm^{-1} that correspond respectively, to the transverse acoustic (TA), longitudinal acoustic (LA) and transverse optical (TO) modes of ZrN. Additionally, three broad bands observed at around 400 cm^{-1}, 700 cm^{-1} and 1085 cm^{-1} were attributed to the second-order acoustic (2A), LA + TO and 2TO modes of ZrN [39,40]. According to Mokgadi et al. [41] defect-free ZrN has the face-centered cubic NaCl structure with every atom at the site of inversion symmetry and therefore presenting no vibrational modes, thus every Raman modes observed in the spectrum are defect-induced modes. The distinctive acoustic modes are associated

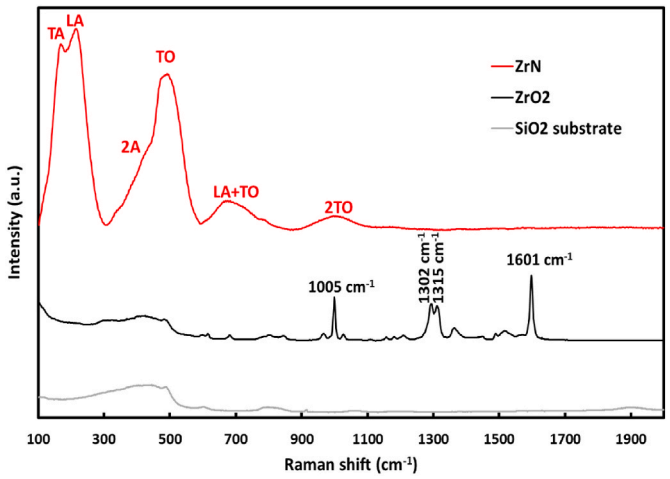

Fig. 4. Raman spectra of the SiO_2 substrate, ZrO_2 xerogel, and ZrN thin films.

with zirconium vacancies, whereas the optical modes are indicative of nitrogen vacancies. The presence of second-order acoustic modes suggests a ZrN composition with fewer stoichiometric defects [42]. These Raman peaks are characteristic of ZrN thin films [39,40,42,43] even though shifts are observed. The nitridation process used to produced ZrN induce multiple defects in the layer. Indeed, the very fast process produces to a disordered and constrained ZrN crystal structure that can leads to a shift of the peaks. The Raman spectrum presented in the study of Spengler et al. [37] and Constable et al. [40] exhibit a very similar peaks placement but the resolution of the TO, LA + TO and 2TO peaks do not allow the precise determination of their position. The main difference in mode detected is the much less detectable 2A modes and the absence of the LO mode. According to Mokgadi et al. [41] and Constable et al. [42] the appearance of second-order acoustic modes is an indication of ZrN with less stoichiometric defects. Thus, as expect, this would mean that the ZrN thin film produced present more stoichiometric defects then Mokgadi et al. [41] (deposited by vacuum arc deposition).

The diffractogram of the ZrO_2 xerogel layer obtained by GIXRD displayed no peaks, thereby confirming the amorphous nature of the ZrO_2 xerogel film before nitridation (black curve in Fig. 5). The diffractogram obtained from the nitridated ZrN thin film (red curve in Fig. 5) displayed five characteristic peaks centered respectively at angles 2θ equal to 34.02, 39.50, 57.10, 68.14 and 71.74°. After background subtraction, their relative intensities normalized to the most intense peak (39.50°) were 95.9, 100.0, 58.1, 39.8 and 18.2%. A Bragg index was applied using the COD database [44]. The most probable phase in agreement with the diffractogram is the cubic phase $Fm\bar{3}m$ (225) of the

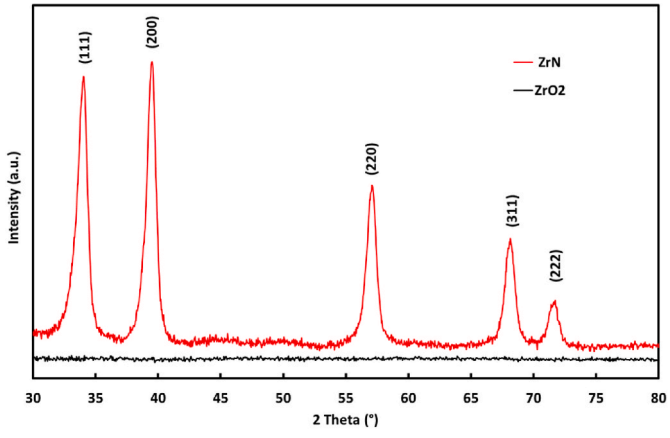

Fig. 5. GIXRD patterns for an amorphous ZrO_2 xerogel and ZrN thin film.

ZrN, with a cell parameter of 0.4563 nm. The diffraction peaks within the diffraction range investigated correspond to the crystalline planes (111), (200), (220), (311), (222).

Table 1 compares the values of inter-reticular distance $d_{(hkl)}$ and relative intensity of the peaks (I) deduced from the GIXRD measurements of the ZrN layer and the reference extracted from the COD data base [40]. The values of $d_{(hkl)}$ measured agree with the literature, the relative error calculated for each crystal plane never exceeded 0.5%. The minor shift in the inter-reticular distances could be caused by internal stresses but this quantification was not yet done [41]. Considering the instrumental width of the X-ray signals deduced from the diffractogram of the LaB6 reference powder in acquisition conditions resemble those used for ZrN, the sizes of the ZrN grains computed from the Scherrer equation are respectively 17.6 nm, 22.7 nm and 25.2 nm, as deduced respectively from the (111), (200) and (220) diffraction peaks located below $2\theta = 65°$. Thus, the mean size of the ZrN grains deduced from GIXRD was 22 nm (±3 nm). Such grain sizes were confirmed by TEM images, as shown in Fig. 6A.

The presence of crystals of ZrN was confirmed by HRTEM diffractograms (Fig. 6B). The measurement corroborates the presence of a ZrN crystalline phase with a face-centered cubic (fcc) structure and a unit cell length of 0.4563 nm [44]. EELS experiments were performed on a slice of a ZrO_2 xerogel and a ZrN layer. To be sure the probed volume was similar in the ZrO_2 xerogel and ZrN samples, the thickness of the ZrO_2 xerogel sample was reduced from 250 nm to 100 nm. The edge used for the analyses were the Zr $L_{2,3}$ edge at 2222 and 2307 eV, the N K edge at 402 eV, the O K edge at 532 eV and the Si K edge at 1839 eV. For better visibility, the energy loss spectra were vertically translated and the range between 1700 and 2400 eV was multiplied by 25. The EELS measurement of the ZrO_2 xerogel layer in Fig. 7A shows homogeneous presence of Zr and O in the layer and a strong presence of Si and O in the substrate, as expected. No trace of nitrogen was detected before nitridation as there was no characteristic peak in the energy loss spectrum. As expected, the EELS measurement of the ZrN layer in Fig. 7B confirms the homogeneous presence of Zr and N in the film and the strong presence of O in the SiO_2 substrate. Nevertheless, oxygen was detected in several areas on the ZrN film, as can be seen on the O map. Concerning the weaker intensity of the O K edges in this region and the protective FIB layers, one can reasonably assume that both the top surface of the ZrN layer and the entire surface of the FIB lamella are contaminated by ambient oxygen following the nitridation process and the final FIB lamella step, respectively. EELS data provided further evidence that the layer was completely nitrided in the form of ZrN following the nitridation process.

3.2. Properties of ZrO2 xerogel and ZrN films

3.2.1. Optical properties

The refractive index n and the extinction coefficient k of the ZrO_2 xerogel thin films measured by spectroscopic ellipsometry before and after the nitridation are reported in Fig. 8A and B, respectively. The value of the refractive index (n) in ZrO_2 xerogel decreased with an increase of the wavelength in the visible range, while the extinction

Table 1
Experimental $d_{(hkl)}$ and relative intensity I (%) of the zirconium nitride film investigated, compared to the $d_{(hkl)}$ and I (%) values reported for ZrN in the literature [43].

	(111)	(200)	(220)	(311)	(222)
$d_{(hkl)}$ experimental (nm)	0.2632	0.2278	0.1611	0.1374	0.1314
$d_{(hkl)}$ literature (nm)	0.2642	0.2284	0.1614	0.1376	0.1317
$(d_{experimental} - d_{literature})/d_{literature}$ (%)	−0.4%	−0.25%	−0.21%	−0.15%	−0.28%
I (%) experimental	95.95	100.00	58.08	39.79	18.17
I (%) literature ZrN	94.45	100.00	40.17	38.27	15.64

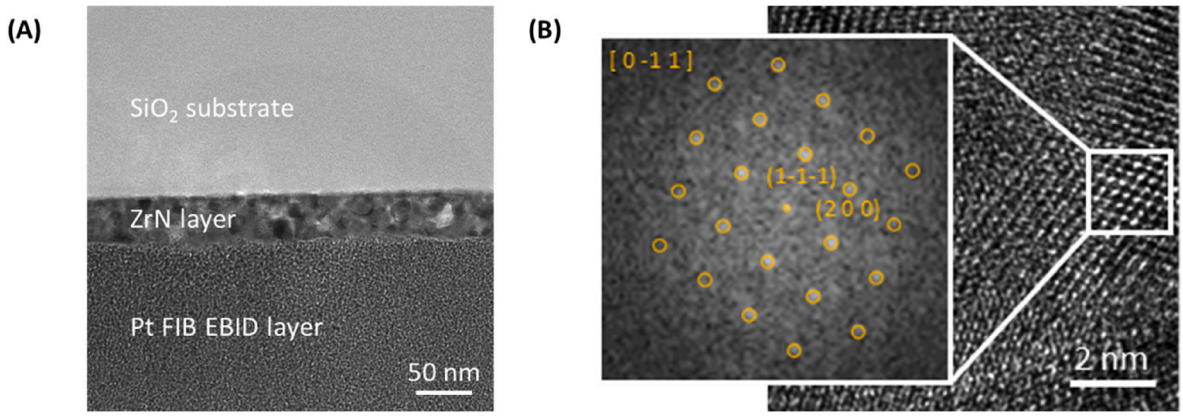

Fig. 6. (A) Cross-sectional TEM image of the ZrN thin film. (B) HR-TEM image of the same ZrN layer. Inset: corresponding fast Fourier transform (FFT) showing the (1-1-1) and (200) directions of ZrN FCC structure in the [0−1 1] zone axis.

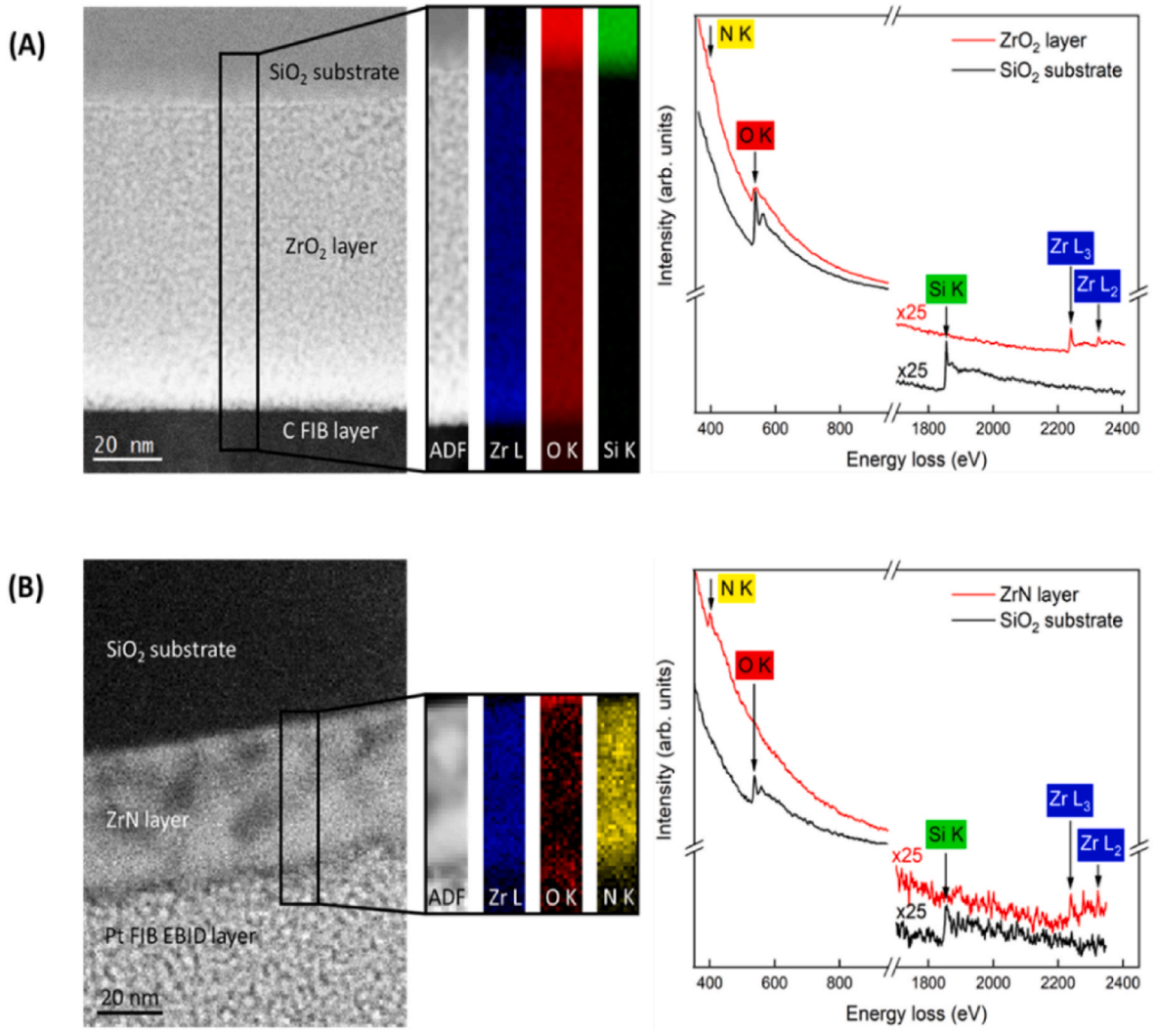

Fig. 7. (A) Left: Cross-sectional HRTEM of ZrO_2 xerogel thin film, annular dark field (ADF), element mapping images of Zr, O and N. Right: corresponding EELS spectra of SiO_2 substrate and ZrO_2 xerogel layer. (B) Left: Cross-sectional HRTEM of ZrN thin film, annular dark field (ADF), element mapping images of Zr, O and N. Right: corresponding EELS spectra of SiO_2 substrate and ZrN layer.

coefficient (k) dropped to zero above 420 nm, confirming the good transparency of ZrO_2 xerogel above this wavelength, as expected. The shape of the curve representing ZrN is quite different (solid lines in Fig. 8B). The refractive index n of ZrN decreases up to 500 nm then increases with an increase in the wavelength and was 3.5 at 950 nm, while the extinction coefficient did not reach a zero value over the whole range, confirming the absorption of the ZrN film. These results resemble those in the literature, with a slight difference that can be explained by

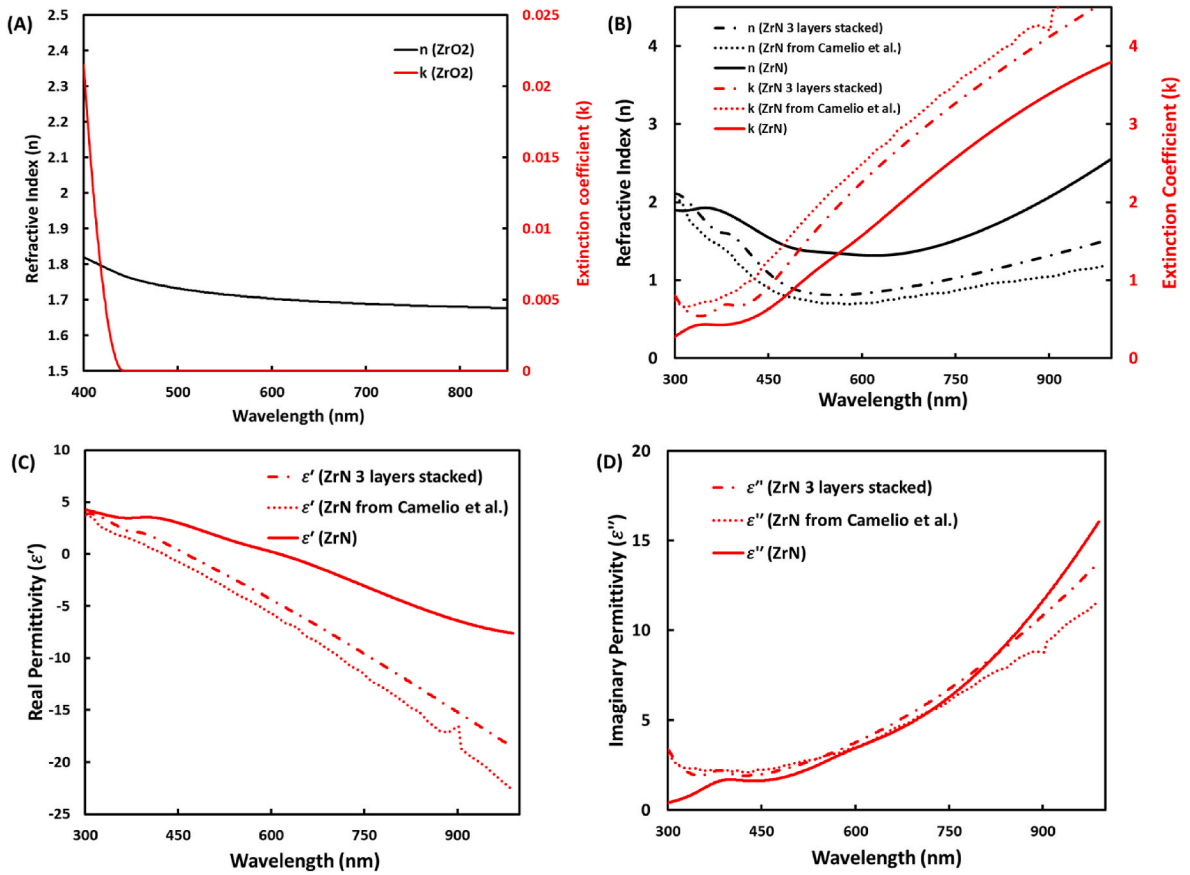

Fig. 8. Refractive index (n), extinction coefficient (k) spectra of amorphous ZrO_2 xerogel (A) and ZrN (B) thin films. Permittivity according to the wavelength for a ZrN film (C) real part and (D) imaginary part. These values are compared with the values reported by Camelio et al.

the porosity and the roughness of the ZrN layer caused by the sol-gel process [31]. Indeed, it was shown that the increase in porosity and roughness of a film significantly reduces the extinction coefficient, as can be seen in Fig. 8B [45,46]. Furthermore, the ZrN sample thickness makes difficult the comparison with the literature. To get around this difficulty, samples with 3 stacked layers of ZrN were produced by repeating the process of deposition and nitridation of ZrO_2 xerogel on the same sample 3 times. As can be seen in Fig. 8A and B, the refractive index and the extinction coefficient are much closer to those in the literature.

The thickness of the ZrN layer deduced from the ellipsometric measurements was 46 nm, as expected from the cross-sectional TEM image (Fig. 6A) and the profilometer measurements. The thickness of the 3 stacked layers of ZrN was 82 nm according to the ellipsometric measurements.

The real and imaginary part of the permittivity were computed from the ellipsometric measurements using eq. (1) below, and are shown in Fig. 8C and D, respectively:

$$\varepsilon' = n^2 - k^2 \; \varepsilon'' = 2nk \tag{1}$$

The real permittivity can be considered as an indicator of the metallic properties of the ZrN layer. The metallic properties improve with increasing absolute value of the real permittivity. In our case, ZrN reached $\varepsilon' \approx -7$ at $\lambda = 950\,nm$. The imaginary permittivity increased almost linearly with increasing wavelength and was equal to $\varepsilon'' \approx 14$ at $\lambda = 950\,nm$ (Fig. 8C and D). By comparing these values of permittivity with those in the literature [31] we can conclude that the ZrN film

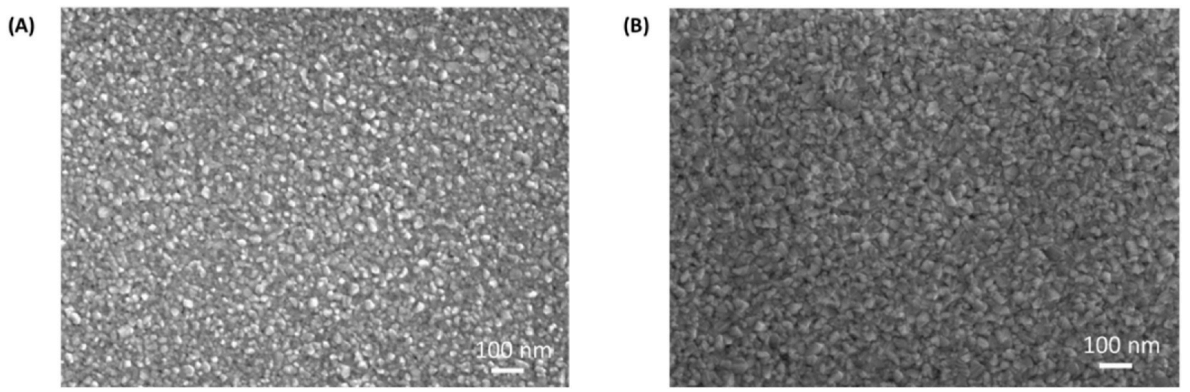

Fig. 9. SEM images of (A) 1-layer ZrN sample and (B) 3-stacked layer ZrN sample.

obtained by RTN exhibits a lower metallic character. Multiple factors can explain the difference in permittivity: the porosity and roughness produced at the surface of the sample (observable in Figs. 6, Figs. 9 and 10) are a consequence of high temperature thermal treatment [47]. Furthermore, the impurity present in the layer and inerrant to the sol-gel nitridation route tend to cause losses on the dielectric properties thus can also explain this difference in matching [48]. It was also proved that sol-gel route induces a higher porosity and a lower density than other film deposition techniques such as PVD [49]. In the case of stacked ZrN layers, real permittivity reached $\varepsilon' \approx -17$ at $\lambda = 950\ nm$ and imaginary permittivity was $\varepsilon'' \approx 12$ at $\lambda = 950\ nm$ (Figure 8C and D). The values obtained with the 3-layer sample are thus closer to those reported in the literature then the values obtained with the 1-layer sample. SEM images of the surface of the 1-layer ZrN and the 3-stacked layers ZrN sample are presented in Fig. 9.

Few open porosities can be seen on the film surface, but the TEM image on cross section in Fig. 6A shows porosities inside the film. As specified previously this porosity is inerrant to the sol-gel route used in this study [47]. Roughness of the sample is also observed Fig. 10. It can be seen that the surface of the 1-layer sample is much rougher than the 3-stacked layer sample. The RMS of the ZrN 1-layer is $R_a = 2.331$ nm while the 3-stacked layer is $R_a = 1.819$ nm. Furthermore, the ratio between the thickness of the layer and the roughness is much higher for the ZrN 1-layer.

Both a diminution of porosity and the roughness have for consequence the enhancement of the metallic property. Another reason that can explained this difference involves the thickness of the films. Indeed, with only one layer, the thickness is very low (40 nm) and the film is not completely uniform. Stacking the layers should considerably improve uniformity thereby also improving the optical constant. Nevertheless, the one-layer ZrN presented here can be considered a metallic material and optimizing the RTN parameters could improve the performances of the ZrN layers produced. Further studies on the influence of the nitridation parameters and the stacking of the layers are required to understand their impact on the refractive index and the extinction coefficient.

3.2.2. *Electrical properties*

Electrical measurements were taken on the ZrO_2 xerogel and ZrN films and the results are listed in Table 2 with values reported in the literature for comparison. The ZrO_2 xerogel film exhibits dielectrical properties with high resistivity of $4.9 \times 10^5\ \Omega.cm$. According to the literature, resistivity values can vary widely from 10^4 to $10^{12}\ \Omega.cm$ as a function of the technique and of the deposition parameters [50–52]. The value measured in the ZrO_2 xerogel film is one order of magnitude higher than the least resistive ZrO_2 cited in the literature.

After nitridation, the ZrN layer showed much lower resistivity: $1.22 \times 10^{-2}\ \Omega.cm$. This result is far from any result reported in the literature ($6.13 \times 10^{-2}\ \Omega.cm$) but the resistivity of the sample with 3 stacked layers is much closer ($3.70 \times 10^{-4}\ \Omega.cm$). Thus, the addition of ZrN layers improves the metallic properties of the ZrN film, in agreement with ellipsometry measurements. As presented in the Figs. 9 and 10 the thinness, porosity and roughness of the monolayer tend to degrade the film's conductivity compared with a 3-stacked layer sample.

However, the resistivity of the 3 layer sample is still about one order of magnitude higher than values reported in the literature [53]. This difference can be attributed both to the thickness of the film [53] and to the method of preparation. Indeed, films prepared using the sol-gel route

Table 2
Resistivity measurements of ZrO_2 xerogel and ZrN thin films.

	Resistivity ($\Omega.cm$)	Thickness (nm)
ZrO_2 xerogel	4.9×10^5	250
ZrO_2 (literature) [50–52]	10^4 to 10^{12}	/
ZrN	1.22×10^{-2}	40
ZrN (3 layers stacked)	3.70×10^{-4}	90
ZrN (literature) [53]	6.13×10^{-5}	160

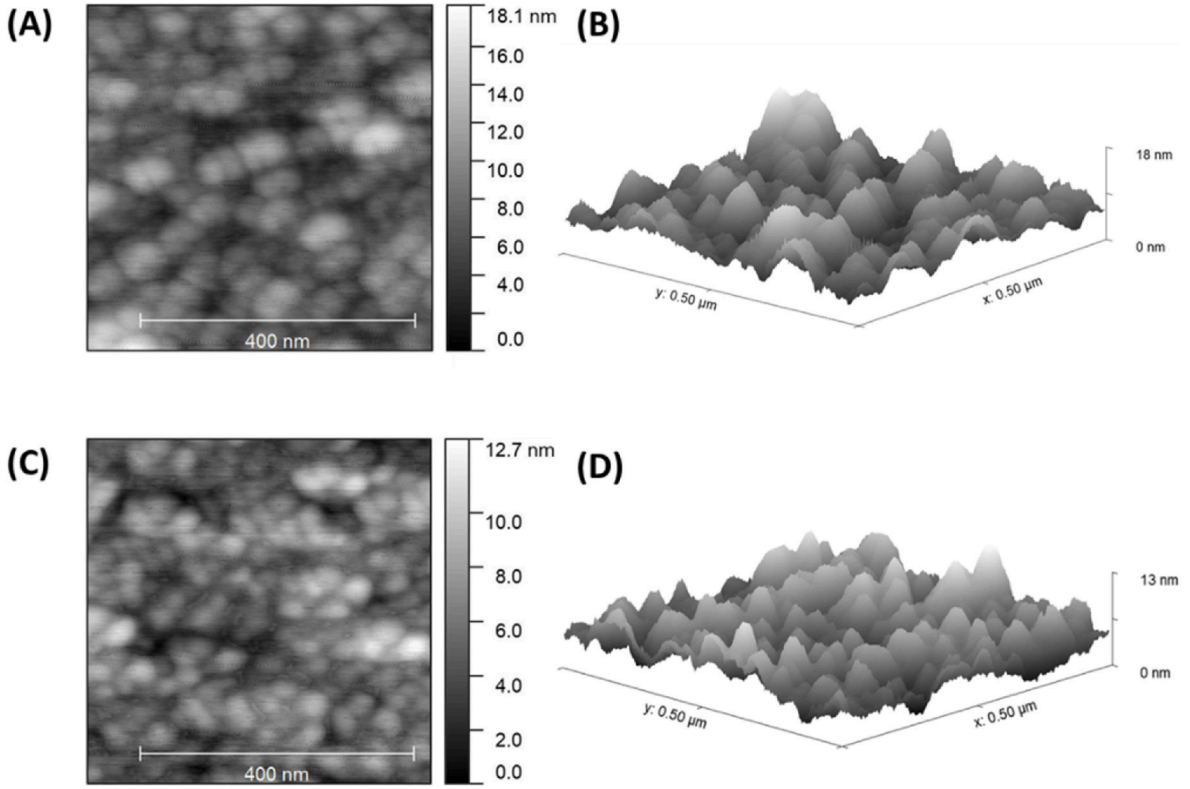

Fig. 10. (A) AFM image and (B) 3D representation of the ZrN 1-layer. (C) AFM image and (D) 3D representation of the ZrN 3-stacked layer.

are generally less dense than films obtained by physical deposition.

3.2.3. Friction properties

Fig. 11 shows changes in the friction coefficient as a function of the number of sliding cycles of the ZrN film tested against the stainless-steel ball in reciprocating sliding contact. The friction coefficient remained remarkably stable at a relatively average value of 0.11 during the 100 sliding cycles. Such a friction coefficient range is slightly lower than values related to typical ZrN films deposited by magnetron sputtering: Auger et al. observed friction coefficients in the 0.17–0.22 range, but at a higher average contact pressure of 667 MPa than that used in our conditions (266 MPa) [54]. Indeed, the normal force used by these authors was 1 N, the same as in our experiment, but their ZrN film was deposited on a silicon substrate and friction was performed with a smaller steel ball, whose diameter was only 3 mm. According to the Hertzian contact model, these differences are responsible for a higher average contact pressure.

The inset in Fig. 11 shows one extremity of the linear wear track, which appears remarkably smooth, with little accumulation of wear debris at the turning point of the reciprocating motion. The wear track width is in the 100 μm range, which is in the same order of magnitude as the 70 μm corresponding to the theoretical contact width according to the Herztian model.

The friction test showed that our ZrN film exhibits low dry friction with negligible wear at the scale of the 100 sliding conditions. Longer tribological tests would be necessary to quantify the wear resistance of the ZrN film with a view to using it as a solid lubricant.

3.2.4. Micro-nanostructuring of ZrN films

The photo-structurability of the ZrO_2 xerogel enables easy production of micro-nanostructured ZrN films after nitridation. In the following section, we demonstrate the complete process of structuration of ZrN film from this sol-gel using colloidal lithography. The main advantage of this technique is that it makes possible and easy the structuring ZrN coating on planar and non-planar surfaces of varying surface area. For the purpose of this article, nanopillars were produced using this technique. To obtain the nanopillars, a monolayer of silica microspheres with a diameter of 2.5 μm was deposited on the ZrO_2 xerogel film (Fig. 2F). The sample was then illuminated with UV light at a wavelength of 365 nm for 120 s at an intensity of 105 mW cm^{-2}. The exposed film was then developed by immersing it in ethanol for a few seconds, and then rinsing it in deionized water.

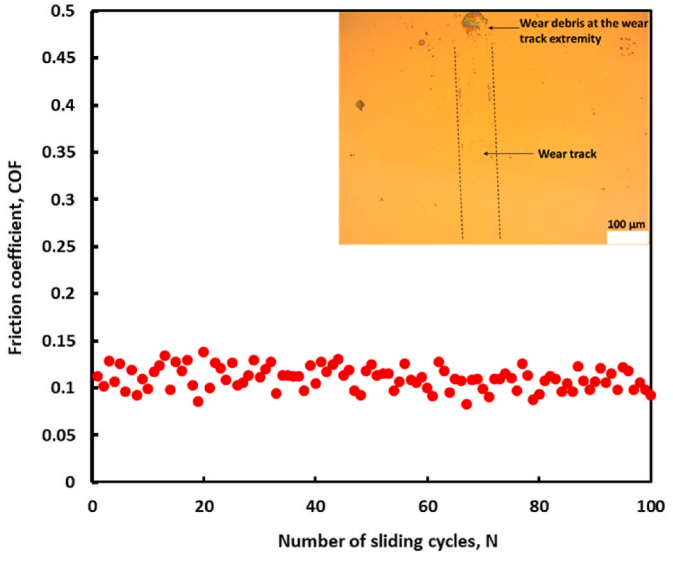

Fig. 11. Friction coefficient evolution, versus the number of sliding frictions, of the ZrN film in reciprocating sliding contact against a stainless-steel ball. Inset: optical micrograph of one extremity of the ZrN wear track.

The SEM and AFM images (Fig. 12A and B) show a hexagonal structure of ZrO_2 xerogel nanopillars with a period of (2.5 ± 0.2) μm as can be deduced from the FFT of the SEM images. The mean diameter and height of these pillars, determined from the AFM measurements as presented Fig. 12B, were respectively, (1.0 ± 0.2) μm and (500 ± 50) nm. After nitridation using the same process as described above (RTN treatment of 10 cycles, each cycle comprising 30 s of high irradiation and 5 s of low irradiation), measurements were made using SEM and AFM. As can be seen in Fig. 12C and D, the hexagonal structure was also conserved using a similar period of (2.5 ± 0.2) μm. The mean measured diameter and height of the ZrN pillars were respectively, (0.6 ± 0.1) μm and (140 ± 20) nm. During the nitridation process a shrinkage of about 45% in diameter and 70% in height occurred. Thus, despite this expected shrinkage the RTN process can be applied on structured ZrO_2 xerogel layer without damaging the patterns.

AFM analysis of the 2D hexagonal grating profile in Fig. 12A and D illustrate a non-perfect rectangular 2D grating shape and one can observe a “V shape” from both side of the circular pillars, like teeth. Such a shape was previously reported and investigated by the authors on 1D grating profile [55]. This grating profile’s modification is explained by the annealing process at high temperature and the densification of the xerogel layer. The annealing process induces the xerogel layer densify and reduce the layer thickness. In the case of a 2D grating patterning with circular pillars, the densification occurs on the grating pillars and is not homogenous in all the directions due to the adhesion of the pillars on the substrate which makes mechanical constraints. This makes a non-homothetic reduction of the pillars and the densification of the xerogel is thus amplified in the center of the grating pillars and reduced of the pillars flanks to form this “V shape” or teeth effect.

4. Conclusion

This paper presents a new, innovative method to rapidly and easily produce ZrN films on a flat or non-planar surface of different areas thanks to the ZrO_2 sol-gel solution used. After 15 min of RTA treatment in an ammonia atmosphere, the conversion of ZrO_2 xerogel into ZrN was shown. Indeed, UV–visible–NIR spectroscopy showed an increase in reflectivity in the infrared range after nitridation of the ZrO_2 xerogel layer and characteristic peaks of ZrN were observed by Raman spectroscopy. The structural transformation that occurred during the RTN was also exhibited by GIXDR and HRTEM indicating the complete and homogeneous conversion of the ZrO_2 xerogel thin film into a ZrN thin film. EELS results revealed extremely low oxygen content, confirming that the resulting film is indeed a ZrN layer with low impurity.

The optical, electrical and mechanical properties of the ZrO_2 xerogel and ZrN films were then compared. The ellipsometry and the resistivity measurements showed the results closely resembled those of pure ZrN obtained using the usual deposition technique. However, these results are in the lower range of the values reported in the literature. These differences can be explained by the residual porosity inherent to the sol-gel route, present in the layer and the low thickness of the final ZrN deposit. Further studies are thus needed to overcome these remaining issues. The film displayed typical solid lubricant behavior with little wear. The possibility to produce ZrN micro-nanostructure in a short period of time was also demonstrated: SEM and AFM measurements allow to compare the micro-nanostructure of the film before and after the nitridation. Thus, the method presented here has some major advantages including its easiness to setup, its low price and its rapidity (the RTN takes a few minutes rather than the several hours required for the usual nitridation process). This technology has the potential to achieve very high quality ZrN thin films that could be deposited on non-planar substrates and is promising for a wide range of applications in which the ZrN is used e.g. biomedical applications [56,57], decorative and protective coatings [58] and as a diffusion barrier in microelectronics [59] The possibility of structuring the layers opens the way for other

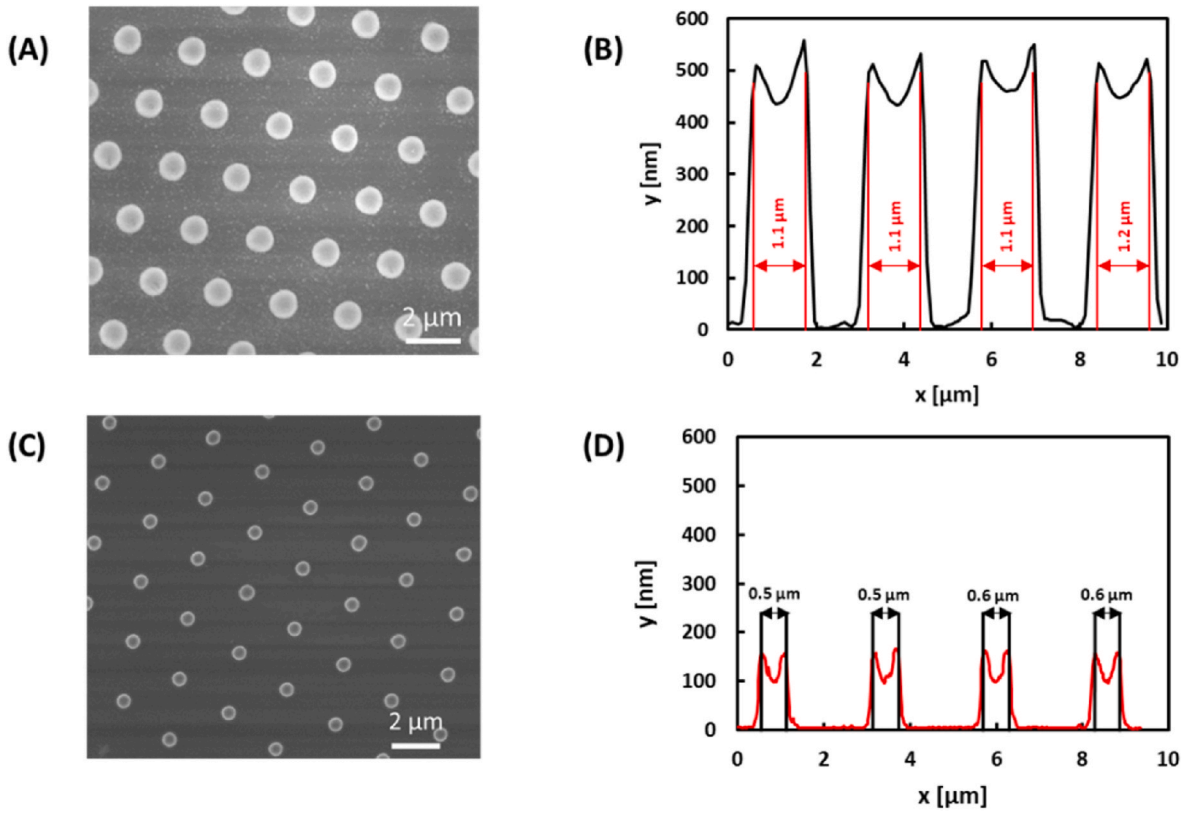

Fig. 12. (A) SEM image and (B) AFM profile of structured ZrO_2 xerogel. (C) SEM image and (D) AFM profile of structured ZrN.

applications such as plasmonic sensors and metasurfaces in extreme environments [2].

Credit author statement

Victor Vallejo-Otero: Conceptualization, Methodology, Investigation, Writing - Original Draft, Writing - Review & Editing, Visualization, Nicolas Crespo-Monteiro: Conceptualization, Writing - Review & Editing, Supervision, Funding acquisition, Arnaud Valour: Investigation, Christophe Donnet: Investigation, Stephanie Reynaud: Investigation, Nadège Ollier: Investigation, Methodology, Writing - Review & Editing, Jean Pierre Chatelon: Investigation, Yannick Bleu: Investigation, Emilie Gamet: Writing - Review & Editing, Supervision, Yves Jourlin: Supervision, Project administration, Funding acquisition.

Declaration of competing interest

The authors declare that they have no known competing financial interests or personal relationships that could have appeared to influence the work reported in this paper.

Data availability

Data will be made available on request.

Acknowledgements

The authors acknowledge the French National Research Agency (ANR) for financial support in the framework of project NITRURATION (ANR-21-CE08-0042-01), and the Centre National de la Recherche Scientifique CNRS (French RENATECH+, nano-SaintEtienne plateform).

References

[1] Qian Guo, Tianrun Wang, Yuehong Ren, Yujing Ran, et al., Plasmonic properties of nonstoichiometric zirconium nitride, oxynitride thin films, and their bilayer structures, Phys. Rev. Mater. 5 (2021), 065201.
[2] A. Shabani, M. Tsegay Korsa, S. Petersen, M. Khazaei Nezhad, Y. Kumar Mishra, J. Adam, Zirconium nitride: optical properties of an emerging intermetallic for plasmonic applications, Adv. Photonics Res. 2 (2021), 2100178.
[3] P. Patsalas, Zirconium nitride: a viable candidate for photonics and plasmonics? Thin Solid Films 688 (2019), 137438.
[4] S. Khan, M. Mehmood, I. Ahmad, F. Ali, A. Shah, Structural and electrical resistivity characteristics of vacuum arc ion deposited zirconium nitride thin films, Mater. Sci. Semicond. Process. 30 (2015) 486–493.
[5] A. Ul-Hamid, Microstructure, properties and applications of Zr-carbide, Zr-nitride and Zr-carbonitride coatings: a review, Mater. Adv. 1 (2020) 1012–1037.
[6] K. Ashok, B. Subramanian, P. Kuppusami, M. Jayachandran, Effect of substrate temperature on structural and materials properties of zirconium nitride films on D9 steel substrates, Cryst. Res. Technol. 44 (2009) 511–516.
[7] J.S. Becker, E. Kim, R.G. Gordon, Atomic layer deposition of insulating Hafnium and zirconium nitrides, Chem. Mater. 16 (2004) 3497–3501.
[8] S. Bhattacharya, et al., Nanocrystalline ZrN thin film development via atomic layer deposition for U-Mo powder, J. Nucl. Mater. 526 (2019), 151770.
[9] F. Frank, M. Tkadletz, C. Czettl, N. Schalk, Microstructure and mechanical properties of ZrN, ZrCN and ZrC coatings grown by chemical vapor deposition, Coatings 11 (2021) 491.
[10] H. Wendel, H. Suhr, Thin zirconium nitride films prepared by plasma-enhanced CVD, Appl. Phys. Solids Surf. 54 (1992) 389–392.
[11] E. Rauchenwald, M. Lessiak, R. Weissenbacher, R. Haubner, Chemical vapor deposition of ZrN using in situ produced ZrCl4 as a precursor, Ceram. Int. 45 (2019) 9410–9414.
[12] W.C. Russell, Experimental design approach to development of a CVD ZrN coating, J. Phys. IV 5 (1995) 127–134.
[13] Q. Chen, et al., MOCVD growth of ZrN thin films on GaN/Si templates and the effect of substrate temperature on growth mode, stress state, and electrical properties, J. Phys. Appl. Phys. 55 (2022), 404003.
[14] J.-H. Huang, C.-Y. Hsu, S.-S. Chen, G.-P. Yu, Effect of substrate bias on the structure and properties of ion-plated ZrN on Si and stainless steel substrates, Mater. Chem. Phys. 77 (2003) 14–21.
[15] Y.-E. Ke, Y.-I. Chen, Effects of nitrogen flow ratio on structures, bonding characteristics, and mechanical properties of ZrNx films, Coatings 10 (2020) 476.
[16] A. Ul-Hamid, The effect of deposition conditions on the properties of Zr-carbide, Zr-nitride and Zr-carbonitride coatings – a review, Mater. Adv. 1 (2020) 988–1011.

[17] T. Kuznetsova, V. Lapitskaya, A. Khabarava, S. Chizhik, B. Warcholinski, A. Gilewicz, The influence of nitrogen on the morphology of ZrN coatings deposited by magnetron sputtering, Appl. Surf. Sci. 522 (2020), 146508.
[18] E.W. Niu, et al., Influence of substrate bias on the structure and properties of ZrN films deposited by cathodic vacuum arc, Mater. Sci. Eng. 460 (2007) 135–139.
[19] V.N. Zhitomirsky, I. Grimberg, R.L. Boxman, N.A. Travitzky, S. Goldsmith, B. Z. Weiss, Vacuum arc deposition and microstructure of ZrN-based coatings, Surf. Coat. Technol. 94 (1997) 207–212.
[20] B. Fu, L. Gao, Synthesis of nanocrystalline zirconium nitride powders by reduction-nitridation of zirconium oxide, J. Am. Ceram. Soc. 87 (2004) 696–698.
[21] H. Yamamura, M. Yamamoto, K. Kakinuma, Synthesis of ZrN thin film by a new carbothermal nitridation method of sol-gel devired ZrO2, J. Ceram. Soc. Jpn. 113 (2005) 458–461.
[22] A. Valour, et al., Micro–nanostructured TiN thin film: synthesis from a photo-patternable TiO 2 sol–gel coating and rapid thermal nitridation, J. Phys. Chem. C 124 (2020) 25480–25488.
[23] A. Valour, et al., Optical, electrical and mechanical properties of TiN thin film obtained from a TiO2 sol-gel coating and rapid thermal nitridation, Surf. Coat. Technol. 413 (2021), 127089.
[24] N. Crespo-Monteiro, et al., Micro-nanostructured plasmonic TiN layer produced using rapid thermal nitridation of a nanoimprinted TiO2 sol-gel, Opt. Mater. Express 12 (2022) 3846.
[25] S. Ishii, M. Yu, K. Chen, T. Nagao, Observation of plasmoelectric effect in plasmonic zirconium nitride, Adv. Mater. Interfac. 10 (2023), 2201751.
[26] N. Farkas, J.R. Comer, G. Zhang, E.A. Evans, R.D. Ramsier, J.A. Dagata, High-voltage SPM oxidation of ZrN: materials for multiscale applications, Nanotechnology 16 (2005) 262–266.
[27] N. Crespo-Monteiro, et al., Versatile zirconium oxide (ZrO2) sol-gel development for the micro-structuring of various substrates (nature and shape) by optical and nano-imprint lithography, Materials 15 (2022) 5596.
[28] L.Q. Zhu, Q. Fang, G. He, M. Liu, X.X. Xu, L.D. Zhang, Spectroscopic ellipsometry characterization of ZrO2 thin films by nitrogen-assisted reactive magnetron sputtering, Mater. Sci. Semicond. Process. 9 (2006) 1025–1030.
[29] G. He, Q. Fang, J.X. Zhang, L.Q. Zhu, M. Liu, L.D. Zhang, Structural, interfacial and optical characterization of ultrathin zirconia film grown by insitu thermal oxidation of sputtered metallic Zr films, Nanotechnology 16 (2005) 40.
[30] D. Valerini, M.A. Signore, A. Rizzo, L. Tapfer, Optical function evolution of ion-assisted ZrN films deposited by sputtering, J. Appl. Phys. 108 (2010), 083536.
[31] S. Camelio, T. Girardeau, L. Pichon, A. Straboni, C. Fayoux, P. Guérin, Transformation of the semi-transparent into the metallic phase of zirconium nitride compounds by implantation at controlled temperature: the evolution of the optical properties, J. Opt. Pure Appl. Opt. 2 (2000) 442–448.
[32] R. Lamni, E. Martinez, S.G. Springer, R. Sanjinés, P.E. Schmid, F. Lévy, Optical and electronic properties of magnetron sputtered ZrNx thin films, Thin Solid Films 447 (2004) 316–321.
[33] J. Tian, et al., A novel triple-porosity model for fractured-vuggy reservoirs based on Maxwell-Garnett mixing rule, J. Pet. Sci. Eng. 208 (2022), 109362.
[34] P. Petrik, et al., Comparative study of surface roughness measured on polysilicon using spectroscopic ellipsometry and atomic force microscopy, Thin Solid Films 315 (1998) 186–191.
[35] Y. Ding, et al., Improved performance of all-thin-film electrochromic devices with two ZrO_2 protective layers, Ionics 24 (2018) 2427–2434.
[36] U.S. Patel, K.H. Patel, K.V. Chauhan, A.K. Chawla, S.K. Rawal, Investigation of various properties for zirconium oxide films synthesized by sputtering, Procedia Technol 23 (2016) 336–343.
[37] S.N. Basahel, T.T. Ali, M. Mokhtar, K. Narasimharao, Influence of crystal structure of nanosized ZrO2 on photocatalytic degradation of methyl orange, Nanoscale Res. Lett. 10 (2015) 73.
[38] S. Oda, H. Uchiyama, H. Kozuka, Thermoplasticity of sol–gel-derived titanoxanes chemically modified with benzoylacetone, J. Sol. Gel Sci. Technol. 70 (2014) 441–450.
[39] W. Spengler, R. Kaiser, First and second order Raman scattering in transition metal compounds, Solid State Commun. 18 (1976) 881–884.
[40] X.-J. Chen, V. Struzhkin, S. Kung, H. Mao, R. Hemley, A. Christensen, Pressure-induced phonon frequency shifts in transition-metal nitrides, Phys. Rev. B 70 (2004), 014501.
[41] T.F. Mokgadi, M.J. Madito, M. Mlambo, V.A. Skuratov, S.V. Motloung, T. T. Hlatshwayo, Slow and swift heavy ions irradiation of zirconium nitride (ZrN) and the migration behaviour of implanted Eu, Nucl. Instrum. Methods Phys. Res. Sect. B Beam Interact. Mater. Atoms 461 (2019) 63–69.
[42] C.P. Constable, J. Yarwood, W.-D. Münz, Raman microscopic studies of PVD hard coatings, Surf. Coat. Technol. 116–119 (1999) 155–159.
[43] J.Y. Li, Y. Sun, Y. Tan, F.M. Xu, X.L. Shi, N. Ren, Zirconium nitride (ZrN) fibers prepared by carbothermal reduction and nitridation of electrospun PVP/zirconium oxychloride composite fibers, Chem. Eng. J. 144 (2008) 149–152.
[44] S. Gražulis, et al., Crystallography Open Database – an open-access collection of crystal structures, J. Appl. Crystallogr. 42 (2009) 726–729.
[45] Y. Zhao, G.H. Tang, Monte Carlo study on extinction coefficient of silicon carbide porous media used for solar receiver, Int. J. Heat Mass Tran. 92 (2016) 1061–1065.
[46] S. Suter, S. Haussener, Morphology engineering of porous media for enhanced solar fuel and power production, JOM 65 (2013) 1702–1709.
[47] P.-T. Shen, Y. Sivan, C.-W. Lin, H.-L. Liu, C.-W. Chang, S.-W. Chu, Temperature- and roughness-dependent permittivity of annealed/unannealed gold films, Opt Express 24 (2016), 19254.
[48] P.R. West, S. Ishii, G.V. Naik, N.K. Emani, V.M. Shalaev, A. Boltasseva, Searching for better plasmonic materials, Laser Photon. Rev. 4 (2010) 795–808.
[49] Y.J. Guo, et al., Experimental research of laser-induced damage of the monolayer ZrO2 PVD and sol–gel films, Opt Laser. Technol. 40 (2008) 677–681.
[50] Z. Ning-Lin, S. Zhi-Tang, S. Qin-Wo, L. Cheng-Lu, Microstructural and electrical properties of ZrO2 thin films prepared on silicon on insulator with thin top silicon, Chin. Phys. Lett. 20 (2003) 273–276.
[51] K. Apriany, I. Permadani, D.G. Syarif, S. Soepriyanto, F. Rahmawati, Electrical conductivity of zirconia and yttrium-doped zirconia from Indonesian local zircon as prospective material for fuel cells, IOP Conf. Ser. Mater. Sci. Eng. 107 (2016), 012023.
[52] W.S. Chan, C.K. Loh, Electrical conduction of zirconium oxide films, Thin Solid Films 6 (1970) 91–105.
[53] J.-H. Huang, H.-C. Yang, X.-J. Guo, G.-P. Yu, Effect of film thickness on the structure and properties of nanocrystalline ZrN thin films produced by ion plating, Surf. Coat. Technol. 195 (2005) 204–213.
[54] M.A. Auger, J.J. Araiza, C. Falcony, O. Sánchez, J.M. Albella, Hardness and tribology measurements on ZrN coatings deposited by reactive sputtering technique, Vacuum 81 (2007) 1462–1465.
[55] S. Briche, et al., New insights in photo-patterned sol–gel-derived TiO2 films, J. Mater. Sci. 46 (2011) 1474–1486.
[56] M. Azibi, N. Saoula, H. Aknouche, The influence of substrate bias voltage on the electrochemical properties of ZrN thin films deposited by radio-frequency magnetron sputtering: biomedical application, J. Electr. Eng. 70 (2019) 112–116.
[57] C.-E. Tsai, J. Hung, Y. Hu, D.-Y. Wang, R.M. Pilliar, R. Wang, Improving fretting corrosion resistance of CoCrMo alloy with TiSiN and ZrN coatings for orthopedic applications, J. Mech. Behav. Biomed. Mater. 114 (2021), 104233.
[58] P. Das, B. Biswas, K.C. Maurya, M. Garbrecht, B. Saha, Refractory plasmonic Hafnium nitride and zirconium nitride thin films as alternatives to silver for solar mirror applications, ACS Appl. Mater. Interfaces 14 (2022) 46708–46715.
[59] J. Jung, D. Bae, S. Kim, H.-D. Kim, Self-rectifying resistive switching phenomena observed in Ti/ZrN/Pt/p -Si structures for crossbar array memory applications, Appl. Phys. Lett. 118 (2021), 112106.